Suppporting Information

Streamlined cofactor recycling with formate for chemo-enzymatic synthesis

Di Jiang,[#a] Xiangdong Xue,[#a] Maoyuan Lv,[a] Yuanyuan Zhang,[a] Xuan Xiang,[a] Yan Ye,[a] Fangshu Xing,*[a] and Jian Liu*[a,b]

[a]State Key Laboratory of Photoelectric Conversion and Utilization of Solar Energy, Qingdao New Energy Shandong Laboratory, Qingdao Institute of Bioenergy and Bioprocess Technology, Chinese Academy of Sciences, Qingdao 266101, P. R. China.

[b]College of Materials Science and Engineering, Qingdao University of Science and Technology, Qingdao 266042, P. R. China

*Correspondence to: xingfs@qibebt.ac.cn; liujian@qibebt.ac.cn

[#]Both authors contributed equally to this work

Supplementary methods

Chemicals and Materials

All chemicals were used as received unless otherwise specified. 4,4'-Diamino-2,2'-bipyridine (Dpy), 2-hydroxy-1,3,5-benzenetricarbaldehyde (TFP), 2,4-dihydroxy-1,3,5-benzenetricarbaldehyde (DTFP) and 1,3,5-triformylphloroglucinol (TP) were purchased from Jilin Chinese Academy of Sciences-Yanshen Technology Co., Ltd. Nicotinamide adenine dinucleotide (NAD^+/NADH), pentamethylcyclopentadienylrhodium(III) chloride dimer ($[Cp^*RhCl_2]_2$), sodium formate (HCOONa), methanol, ammonium bicarbonate (NH_4HCO_3) and α-ketoglutaric acid were obtained from Aladdin (Shanghai). Glutamate dehydrogenase (GDH) was supplied by Shanghai Yuanye Biotechnology Co., Ltd.

Characterizations

The Fourier-transform infrared (FT-IR) spectra were collected on a Bruker Vertex 70 V spectrometer equipped with an attenuated total reflectance (ATR) accessory. Nitrogen adsorption-desorption isotherms and pore-size distributions were obtained using a Micromeritics ASAP 2460 analyzer. The morphology and microstructure of the samples were examined by scanning electron microscopy (SEM, Hitachi S-4800). Powder X-ray diffraction (PXRD) patterns were recorded on a Rigaku SmartLab 9 kW diffractometer with Cu Kα radiation ($\lambda = 1.5406$ Å), operating at 45 kV and 200 mA with a scan rate of $5^{\circ}\ min^{-1}$. Solid-state ^{13}C cross-polarization magic-angle-spinning (CP-MAS) NMR spectra were acquired on a Bruker ASCEND 500 MHz spectrometer. ^1H nuclear magnetic resonance (NMR) spectra were measured on a Bruker AVANCE III 600 MHz spectrometer. Contact angles were measured using a LAUDA Scientific LSA100 optical tensiometer. X-ray photoelectron spectroscopy (XPS) was performed on LAUDA Scientific LSA100 with Al-Kα X-ray source and the binding energy data were calibrated with a C 1s peak at 284.8 eV. Steady-state photoluminescence (PL) spectra were recorded on a Shimadzu RF-6000 spectrofluorophotometer at an excitation wavelength of 480 nm. Inductively coupled plasma optical emission spectrometry (ICP-OES) was carried out on an Agilent 730 spectrometer. Ultraviolet-visible diffuse reflectance spectra (UV–Vis DRS) and absorption spectra were obtained using a Hitachi U-3900 spectrophotometer. Electron paramagnetic resonance (EPR) signals were detected on a Bruker EMXplus-6/1 spectrometer.

Photoelectrochemical measurements

The photoelectrochemical measurements were collected on a CHl 660E instrument (Shanghai Chenhua Co., Ltd.) by using a three-electrode cell. A 300 W Xenon lamp (PLSSXE300C photochemical reactor, Perfect Light Ltd, Beijing) was utilized as thelight source. The resultant electrode served as the working electrode, with a carbon rod as the counter electrode and an Hg/Hg_2Cl_2 electrode as the referenceelectrode. The 50 mL of 0.5 M Na_2SO_4 solution was used as the electrolyte. The workingelectrode was prepared on a fluorine-doped SnO_2 (FTO) glass. 5 mg of catalyst were dispersed into a mixedsolution of 1 mL H_2O, 1 mL absolute ethanol, 1 mL isopropanol and 20 μL nafion and treated with ultrasound forseveral minutes. The H_2O, absolute ethanol and isopropanol were used as the thedispersing agent and nafion was used as the binder. Finally, 1 mL of the catalyst dispersion was deposited ontothe FTO glass and then dried in air to form the working electrode. The transient photocurrent measurements were carried out in a three-electrode system. The applied potential during the measurements was 0.6 V vs. Hg/Hg_2Cl_2 (pH 7). Identical experimental conditions were used for all three samples to ensure reliable comparison.

Synthesis of COF-1OH

The COF-1OH was synthesized by solvothermal method. Specifically, Dpy (27.9 mg, 0.15 mmol) and TFP (17.8 mg, 0.1 mmol) were placed into a pyrex tube with the addition of 1,3,5-trimethylbenzene (1 mL) and 1,4-dioxane (1 mL). Followed by sonication for 1 min, then 200 μL of aqueous acetic acid (6 M) was added. The mixture was degassed through three freeze–pump–thaw cycles, and then the tube was sealed and kept at 120 ^{o}C in an oven for 3 days without disturbance. After further cooling down to room temperature, the precipitate was collected and washed with tetrahydrofuran, methanol and acetone for several times to get a colorless supernatant. Finally, the red powder (32.5 mg, 80%) was obtained by drying at 60 °C under dynamic vacuum for 12 h.

Synthesis of COF-2OH

The COF-2OH was synthesized by solvothermal method. Specifically, Dpy (55.9 mg, 0.3 mmol) and DTFP (39.0 mg, 0.2 mmol) were placed into a pyrex tube with the addition of 1,3,5-trimethylbenzene (1.5 mL) and 1,2-dichlorobenzene (1.5 mL). Followed by sonication for 1 min, then 300 μL of aqueous acetic acid (6 M) was added. The mixture was degassed through three freeze–pump–thaw cycles, and then the tube was sealed and kept at 120 °C in an oven for 3 days without disturbance. After further cooling down to room temperature, the precipitate was collected and washed with tetrahydrofuran, methanol and acetone for several times to get a colorless supernatant. Finally, the red powder (59 mg, 71%) was obtained by drying at 60 °C under dynamic vacuum for 12 h.

Synthesis of COF-3OH

The COF-3OH was synthesized by solvothermal method. Specifically, Dpy (55.9 mg, 0.3 mmol) and TP (42.0 mg, 0.2 mmol) were placed into a pyrex tube with the addition of 1,3,5-trimethylbenzene (0.15 mL) and 1,4-dioxane (2.85 mL). Followed by sonication for 1 min, then 300 μL of aqueous acetic acid (6 M) was added. The mixture was degassed through three freeze–pump–thaw cycles, and then the tube was sealed and kept at 120 °C in an oven for 3 days without disturbance. After further cooling down to room temperature, the precipitate was collected and washed with tetrahydrofuran, methanol and acetone for several times to get a colorless supernatant. Finally, the orange powder (75.3 mg, 86%) was obtained by drying at 60 °C under dynamic vacuum for 12 h.

Synthesis of COF-xOH-Rhs

A 5 mL methanol suspension containing $[Cp^*RhCl_2]_2$ (0.3, 0.5, 1, 2, or 5 mg) was mixed with 10 mg of COF-xOH. The mixture was stirred in the dark for 12 h, then washed repeatedly with deionized water and methanol. After drying overnight under vacuum at 60 °C, the resulting solid was collected as COF-xOH-Rh. Using COF-3OH as an example, the Rh loading could be tuned from 1.9 to 6.5 wt%. The highest NADH regeneration efficiency was achieved at 3.6 wt% Rh determined by ICP-OES, and this optimized material was used for subsequent performance tests.

Synthesis of COF-3OH-Rh@GDH

To adsorb glutamate dehydrogenase (GDH) for immobilization, 25 mg of COF-3OH-Rh was activated with 25 mL of 100 mM PBS (pH 7.4). Subsequently, 5 mL of GDH solution (1 mg mL^{-1} in 100 mM PBS pH 7.4) was added to the COF suspension and the mixture was stirred overnight at 37 °C. The obtained solid was then washed several times with PBS to remove loosely bound enzyme, affording the COF-3OH-Rh@GDH composite. The protein concentration in the supernatant was determined using the Enhanced BCA Protein Assay Kit (Beyotime). The enzyme content in the supernatant was then calculated based on the standard curve. The final loading amount of COF-3OH-Rh@GDH was 180 mg g^{-1}.

Synthesis of Rh complexes

In a 20 mL Schlenk tube, methanol (8 mL) was degassed by bubbling with nitrogen for 1 min. Dichloro(pentamethylcyclopentadienyl)rhodium(III) dimer ($[RhCp^*Cl_2]_2$, 123.6 mg, 0.20 mmol) was then added. Subsequently, 2,2′-bipyridine (62.47 mg, 0.40 mmol) was introduced, and the reaction was allowed to proceed at room temperature for 2 h under a nitrogen atmosphere. After completion, the solvent was removed under reduced pressure. Anhydrous diethyl ether was added dropwise to the residue to induce precipitation of a yellow solid. The precipitate was collected by vacuum filtration, washed with anhydrous diethyl ether, and dried under vacuum to afford [Cp*Rh(bpy)Cl]Cl as a yellow powder.

The test for NADH regeneration

The NADH regeneration experiments were carried out in a 2.5 mL bottom-irradiated quartz reactor on a PCX-50 multichannel photochemical workstation (Perfectlight, Beijing). A volume of 2.5 mL PBS (0.1 M, pH 7.4) containing 3.5 mg COF-xOH-Rh, 0.25 mmol HCOONa (0.1 M), and 2.5 μmol NAD^+ (1 mM) was used as the reaction mixture. A Vlight multi-channel panel emitting an AM 1.5G solar spectrum was used as the light source for reaction. No pre-equilibration was required before reactions under dark or light conditions. The reaction temperature was maintained at 37 °C by using a low-constant temperature circulating water bath. During the reaction, 50 μL of liquid sample was periodically collected and diluted 40 times with deionized water for UV−vis absorption characterization at 340 nm. The NADH yield was calculated as follows:

$$\text{yield}\ (\%) = \frac{A - A_0}{6.22} \times \text{dilution ratio} \times 100$$

where A is the absorbance at 340 nm at a certain time; A_0 is the absorbance at 340 nm at 0 minute and the molar absorption coefficient (ε) of 1,4-NADH is typically 6220 M^{-1} cm^{-1}. ^{1}H-NMR was used to detect the selectivity of NADH regeneration.

For formate-driven NADH regeneration under dark conditions, all other reaction parameters were kept identical to those used under illumination. For other sacrificial agent systems, the sacrificial agent concentration was 0.1 M, and all other reaction conditions remained the same.

The test for glutamate production

Glutamate synthesis experiments were conducted in a reaction system similar to photocatalytic NADH regeneration. A volume of 2.5 mL PBS (0.1 M, pH 7.4) containing 3.5 mg COF-3OH-Rh@GDH, 0.25 mmol HCOONa (0.1 M), 2.5 μmol NAD^+ (1 mM), 0.05 mmol α-ketoglutaric acid (20 mM, 11.3 mg) and 0.25 mmol NH_4HCO_3 (100 mM, 19.75 mg). n the free GDH control experiment, 2.5 μmol NAD^+ (1 mM) was directly added as the cofactor to drive the enzymatic conversion of α-ketoglutarate to glutamate. A Vlight multi-channel panel emitting an AM 1.5G solar spectrum was used as the light source for reaction. The reaction temperature was maintained at 37 °C by using a low-constant temperature circulating water bath. Reaction solutions (50 μL) were taken periodically out from the reactor. The conversion of α-ketoglutarate and formate in the collected samples was analyzed by a HPLC (Shimadzu LC40D) with an Aminex@HPX-87H Column (300 mm × 7.8 mm), which coupled to photodiode array detector (PDA) detected at 212 nm. The mobile phase was 5 mM H_2SO_4 with a flow rate of 0.6 mL min^{-1}. The column temperature was 40 °C and the injection volume was 10 μL. The yield of L-glutamate was calculated by the conversion of α-ketoglutarate. Within the integrated system for photocatalytic NADH regeneration and enzymatic glutamate production, the calculation methods for TON and TOF based on NADH are as follows:

$$\mathrm{TON} = \frac{n_{\mathrm{glutamate}}}{n_{\mathrm{NADH}}}$$

$$\mathrm{TOF} = \frac{\mathrm{TON}}{t}$$

where is $n_{glutamate}$ the amount of glutamate at time t, n_{NADH} is the amount of NADH in the system, and t is the reaction time.

Cycle stability experiments for COF-3OH-Rh@GDH were conducted six times under the same reaction conditions described above, with each reaction lasting 2 hours. After each reaction, the catalyst was recovered via centrifugation, and washed with PBS (0.1 M, pH 7.4) for subsequent cycles of reactions.

DFT calculations

All structural optimizations and subsequent energy evaluations were conducted using spin-polarized density functional theory (DFT) as implemented in the CP2K package.[1] The exchange–correlation interactions were described within the generalized gradient approximation (GGA) employing the Perdew–Burke–Ernzerhof (PBE) functional,[2] with the inclusion of Grimme's DFT-D3 empirical dispersion correction[3] to properly account for van der Waals interactions. Core electrons were treated using the Goedecker–Teter–Hutter (GTH) pseudopotentials,[4,5] while the valence electrons were expanded using the molecularly optimized double-ζ valence polarization basis set with short-range characteristics (DZVP-MOLOPT-SR-GTH).[6] The Gaussian and plane waves (GPW) method was employed with an auxiliary plane-wave basis set cutoff of 600 Ry to ensure accurate electron density representation. Geometry optimizations were performed using the Broyden–Fletcher–Goldfarb–Shanno (BFGS) quasi-Newton algorithm, with convergence criteria set to a maximum force component below $4.5\times10^{-}4$ Hartree/Bohr. Initial configuration and input file generation for the CP2K calculations were facilitated by the Multiwfn software,[7,8] which was used to define key calculation parameters.

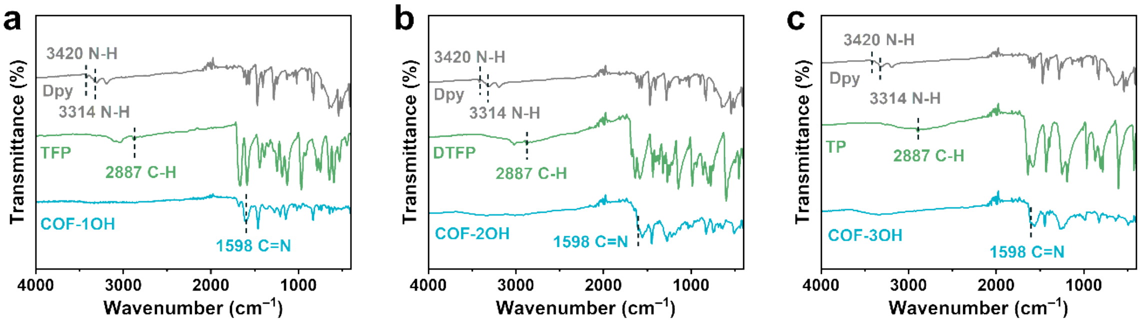

Fig. S1. FT-IR spectra of COF-1OH (a), COF-2OH (b) and COF-3OH (c).

The N–H stretching band (3500–3300 cm^{-1}) for Dpy and the aldehydic C–H stretching vibration peaks (2887 cm^{-1}) for aldehyde monomers disappeared. At the same time, the C=N stretching vibration aroused (1598 cm^{-1}), proving the successful establishment of amine bond in COF-xOHs.[9,10]

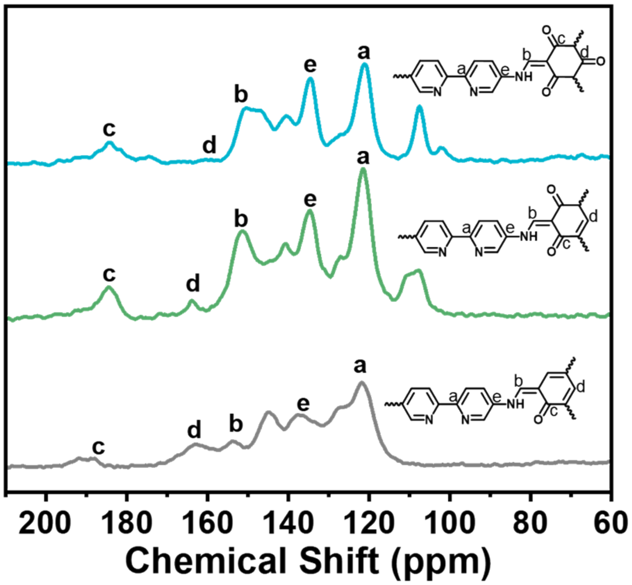

Fig. S2. Solid-state ^{13}C CP/MAS NMR spectra of COF-1OH, COF-2OH and COF-3OH.

The characteristic resonance peak of the imine carbon (marked as b) appears at 150–156 ppm, and the molecular structure of the building blocks remains intact during COF formation, confirming successful condensation of the monomers.[10]

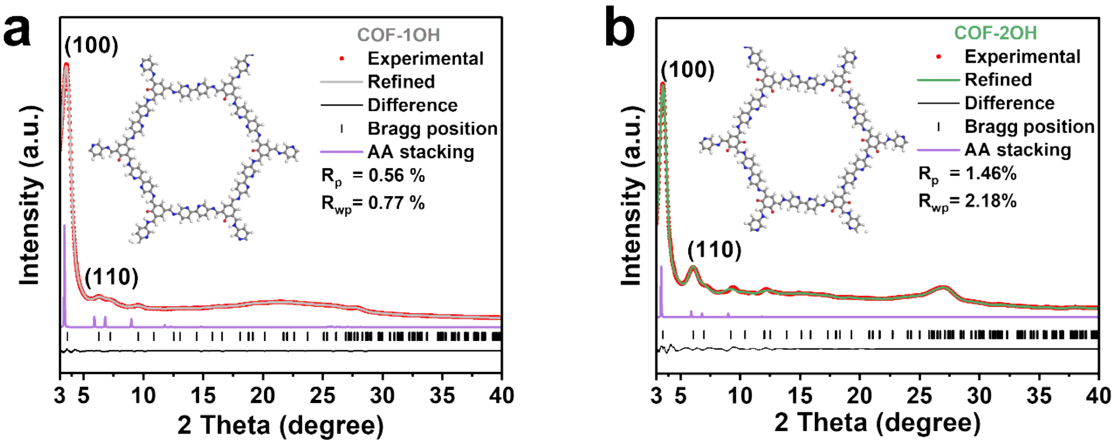

Fig. S3. PXRD patterns of COF-1OH and COF-2OH: experimental patterns (red), Pawly refinement (gray for COF-1OH and green for COF-2OH), simulated pattern for the eclipsed AA stacking model (pink), and refinement differences (black). The inset presents the structural models of COF-1OH and COF-2OH adopting an AA-stacking mode.

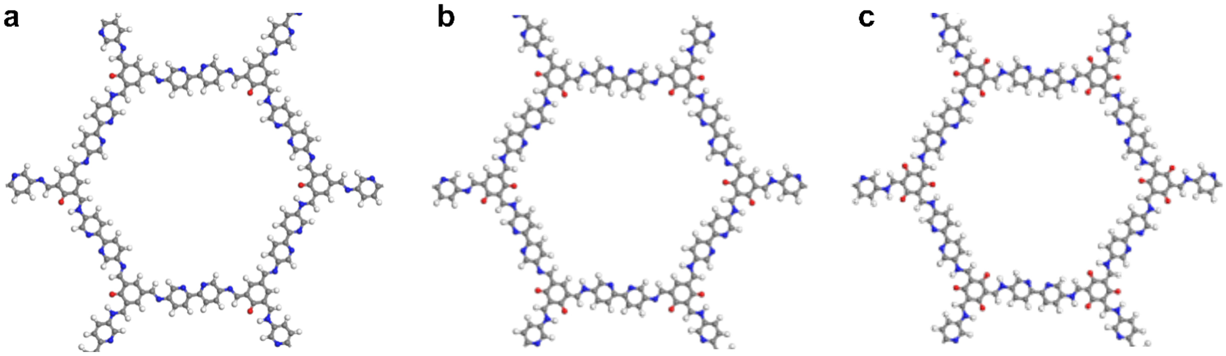

Fig. S4. Top view of the stacking models of COF-1OH (a), COF-2OH (b) and COF-3OH (c). Gray, white, blue, and red spheres represent C, H, N, and O atoms, respectively.

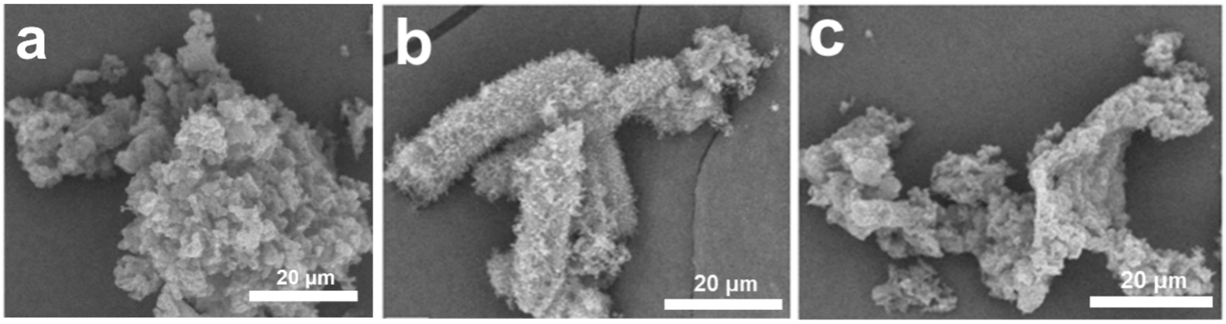

Fig. S5. SEM images of COF-1OH (a), COF-2OH (b) and COF-3OH (c).

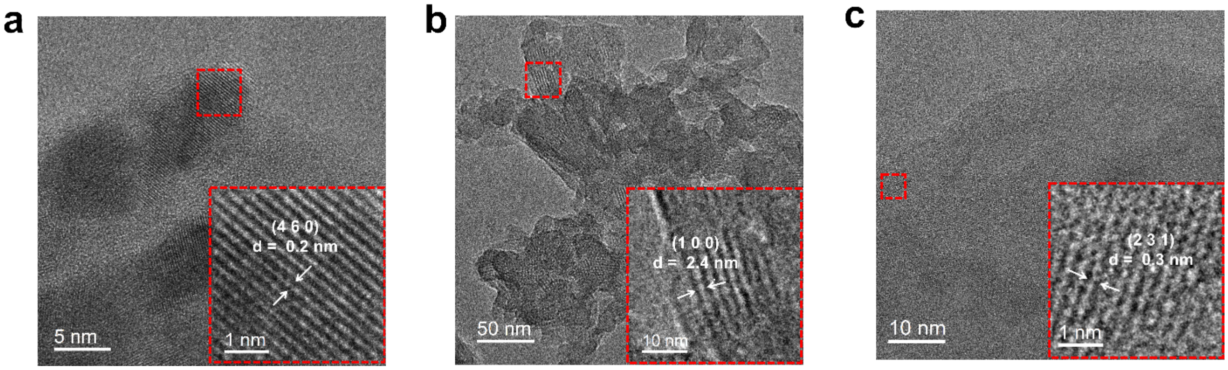

Fig. S6. HRTEM images of COF-1OH (a), COF-2OH (b) and COF-3OH (c).

The HRTEM images of the COF-xOH samples reveal well-defined lattice fringes. The measured interplanar spacings are approximately 0.2 nm for COF-1OH, 2.4 nm for COF-2OH and 0.3 nm for COF-3OH, corresponding to the (460), (100) and (231) crystallographic planes, respectively.

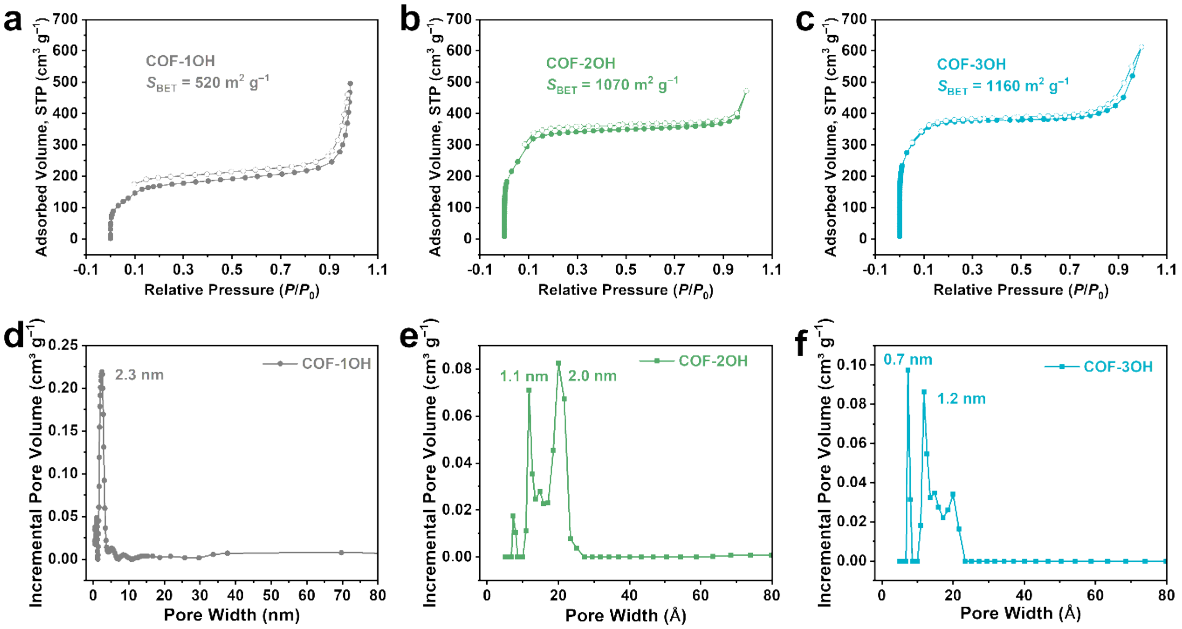

Fig. S7. Nitrogen adsorption–desorption isotherms of COF-1OH (a), COF-2OH (b) and COF-3OH (c). Pore size distribution curves of COF-1OH (d), COF-2OH (e) and COF-3OH (f) calculated using the NLDFT method.

The Brunauer-Emmett-Teller (BET) specific surface areas are 520, 1070 and 1160 m^2 g^{-1} for COF-1OH, COF-2OH and COF-3OH, respectively, consistent with the increasing hydroxyl functionalization.[11] Nitrogen adsorption–desorption isotherms were measured at 77 K for the COF-xOH series. All samples display typical type-I isotherm, featuring a sharp uptake at low relative pressures and subsequent saturation, indicative of their microporous structure. Pore-size distribution analysis reveals that COF-1OH possesses a principal pore size centered around 2.3 nm. In comparison, COF-2OH exhibits bimodal pore sizes at approximately 1.1 and 2.0 nm, while COF-3OH shows even smaller pores, primarily located at 0.7 and 1.2 nm (Fig. S7d–f). The progressive decrease in pore size with increasing hydroxyl content likely results from partial occupation of the pore space by hydroxyl functional groups.[12]

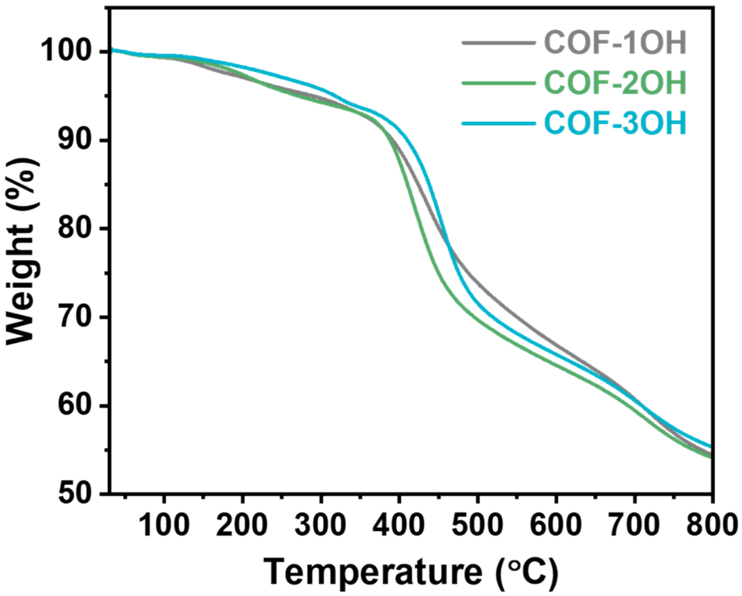

Fig. S8. Thermogravimetric analysis curves of COF-1OH, COF-2OH and COF-3OH.

All three materials can be stabilized in a nitrogen atmosphere up to 400 °C.

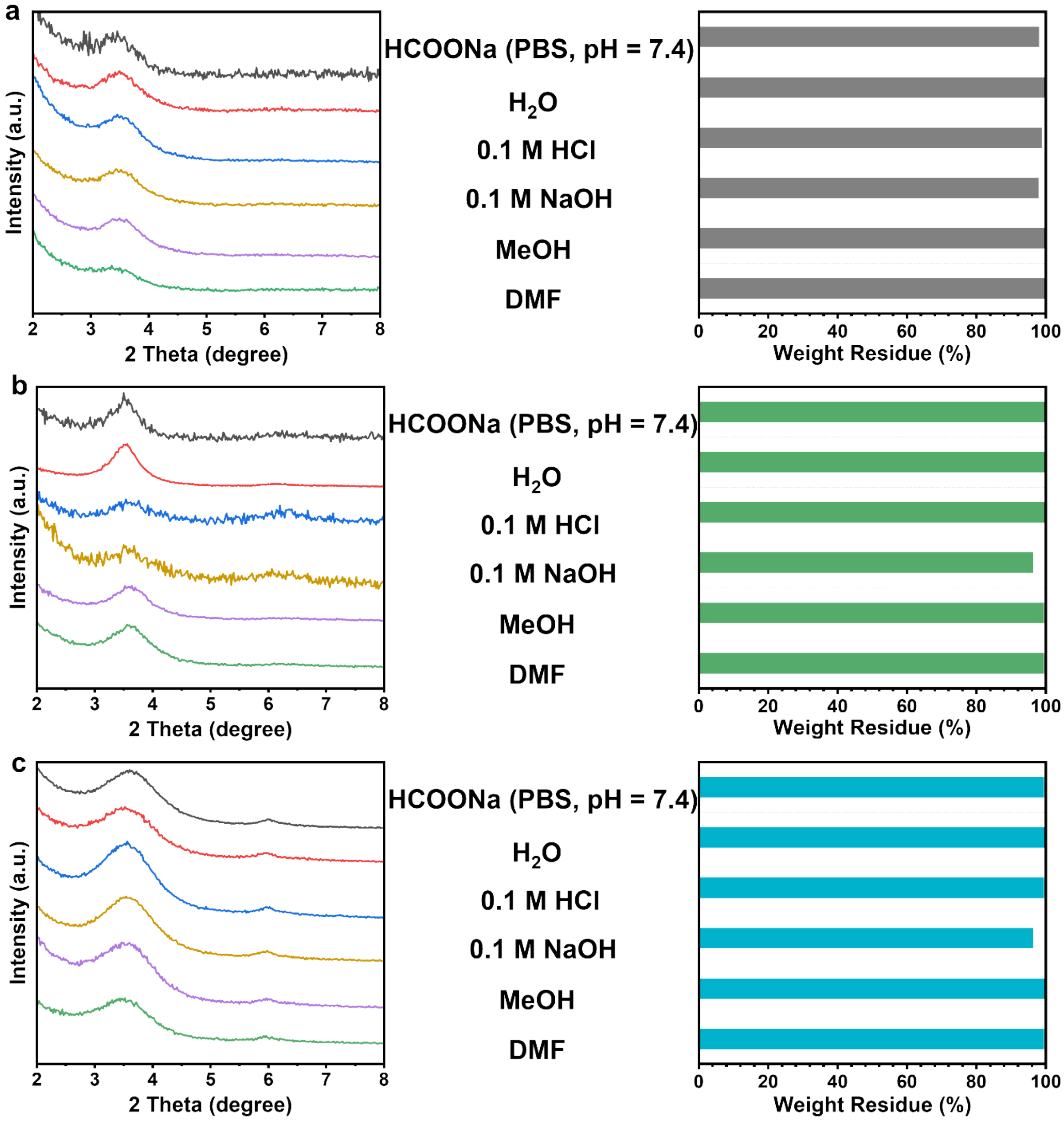

Fig. S9. XRD patterns and residual weight percentages of COF-1OH (a), COF-2OH (b) and COF-3OH (c) after 12 hours of treatment in different solvents.

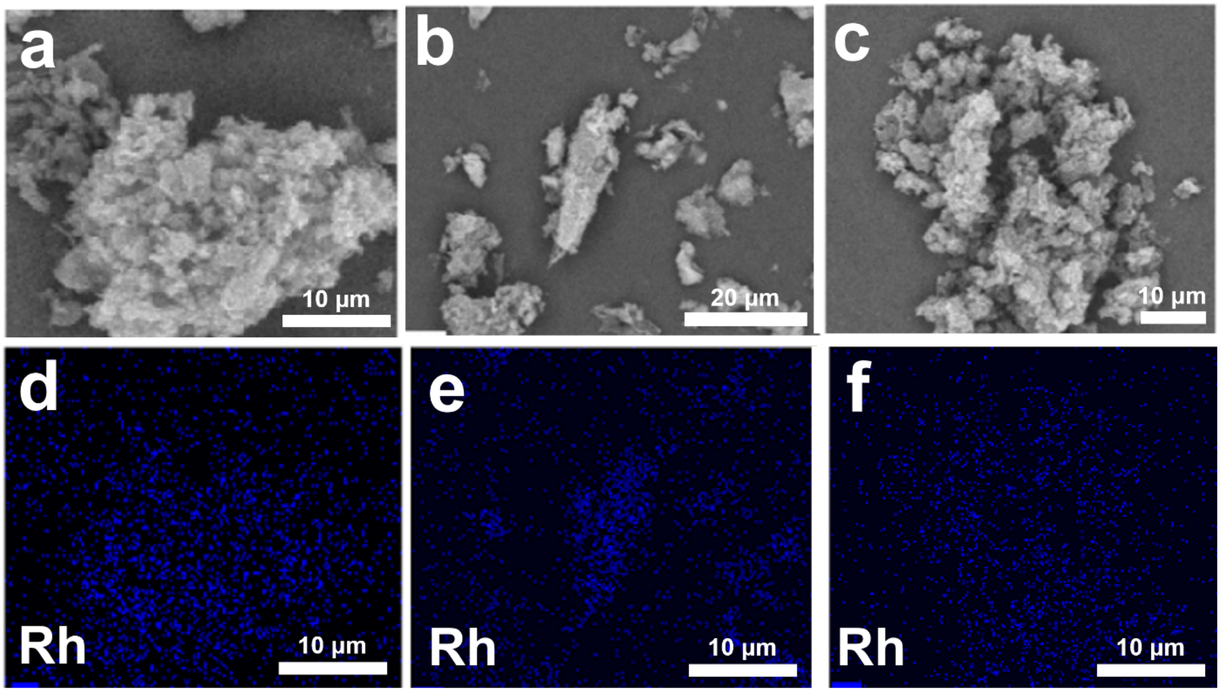

Fig. S10. SEM images of COF-xOH-Rh and corresponding Rh elemental mappings.

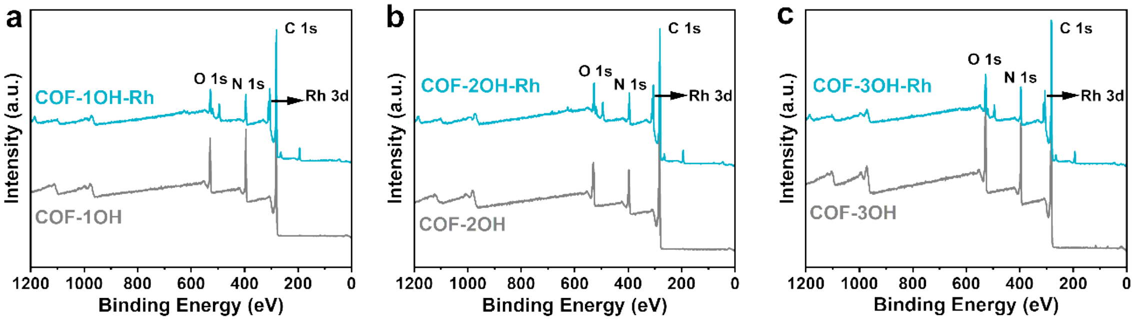

Fig. S11. XPS survey spectra of the COF-xOH and corresponding COF-xOH-Rh samples.

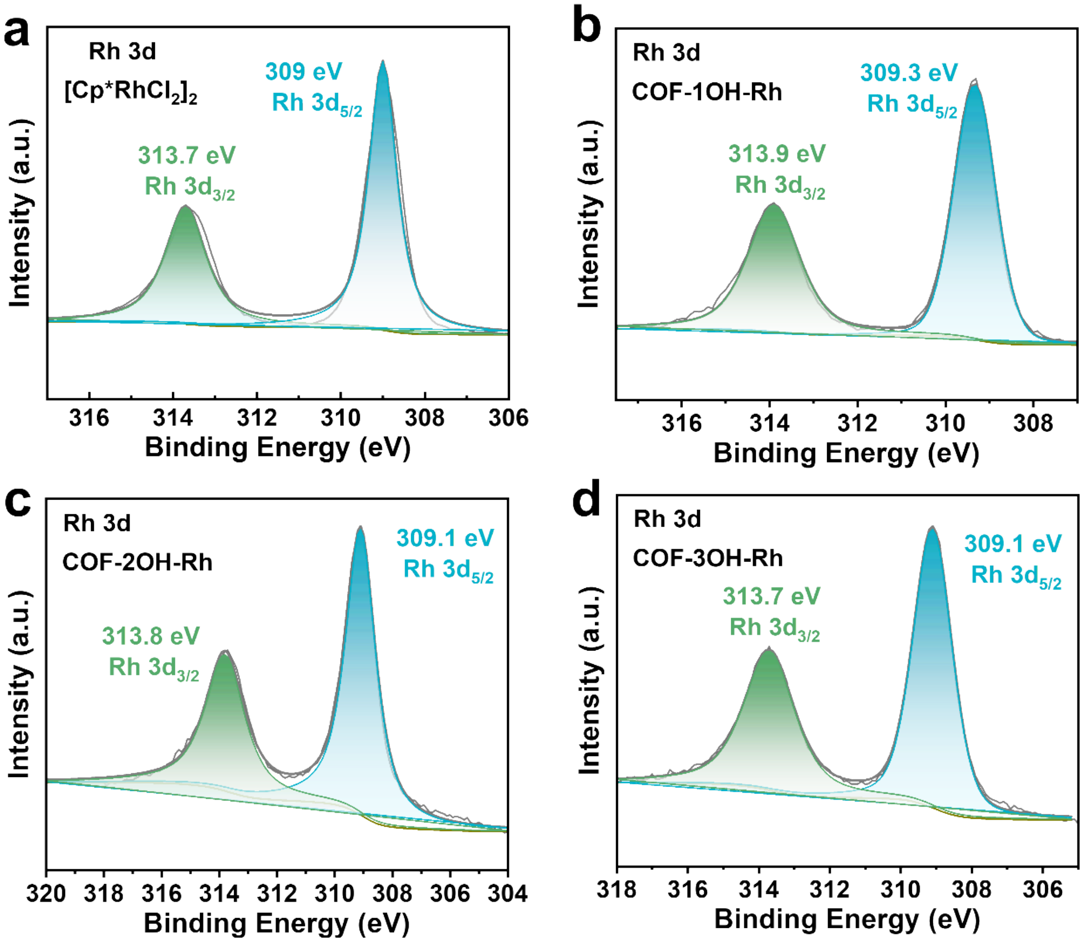

Fig. S12. Rh 3d XPS spectra of [Cp*RhCl$_2$]$_2$ (a), COF-1OH-Rh (b), COF-2OH-Rh (c) and COF-3OH-Rh (d).

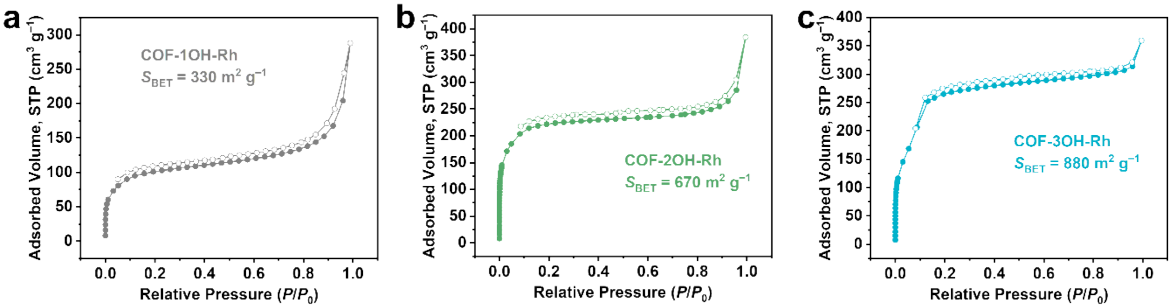

Fig. S13. Nitrogen adsorption–desorption isotherms of COF-1OH-Rh (a), COF-2OH-Rh (b) and COF-3OH-Rh (c).

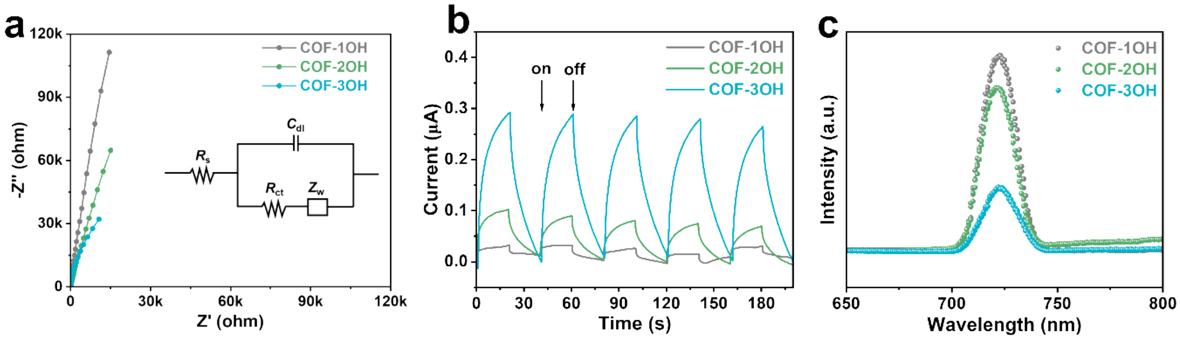

Fig. S14. EIS plots (a), transient photocurrent responses (b) and steady-state PL spectra of COF-xOHs.

The Electrochemical impedance spectroscopy (EIS) plots were analyzed based on an equivalent Randles circuit, including the series resistance (R_s), interfacial charge-transfer resistance (R_{ct}), a constant phase element (C_{dl}) at the electrode–electrolyte interface, and a Warburg element (Z_W) associated with diffusion (Fig. S14a). The R_{ct} values decrease in the order of COF-1OH (734.8 Ω) > COF-2OH (353.8 Ω) > COF-3OH (231.2 Ω). COF-3OH exhibits the lowest charge-transfer resistance, indicating more efficient interfacial electron transfer. Consistent with this, COF-3OH displays a stronger transient photocurrent response under periodic light on-off cycles than the other COFs, reflecting higher charge-separation efficiency (Fig. S14b). Moreover, steady-state photoluminescence (PL) spectra show the weakest emission intensity for COF-3OH (Fig. S14c), suggesting the lowest rate of radiative electron-hole recombination and hence superior potential for photocatalysis. In summary, although the bandgap of COF-3OH is not the smallest (Fig. 1e), it still exhibits the best photocatalytic performance among the three materials.

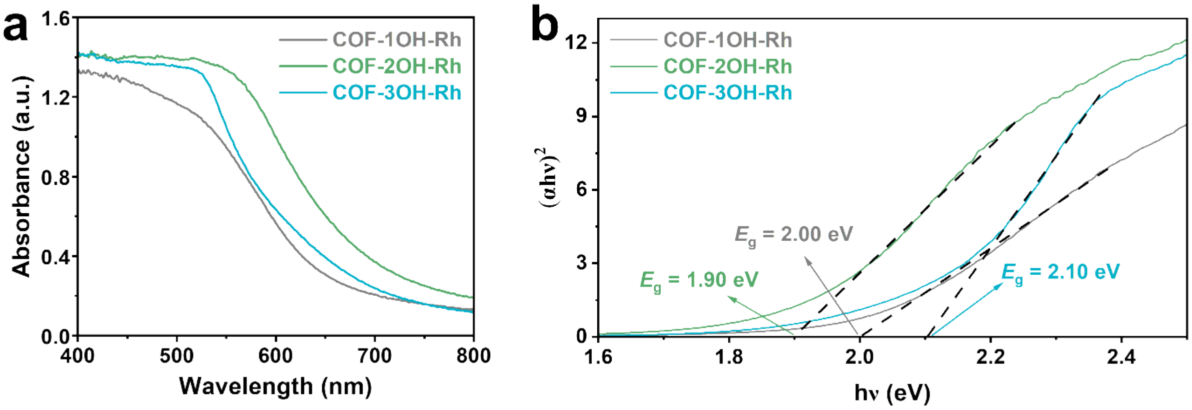

Fig. S15. Solid-state DRS spectra (a) and corresponding Tauc plots (b) of COF-xOH-Rhs.

The solid-state UV–Vis diffuse reflectance spectroscopy (DRS) confirms that the COF-xOH-Rh composites possess broad visible-light absorption (Fig. S15a). Tauc plots derived from these spectra yield optical band gaps of 2.00, 1.90 and 2.10 eV for the series (Fig. S15b).

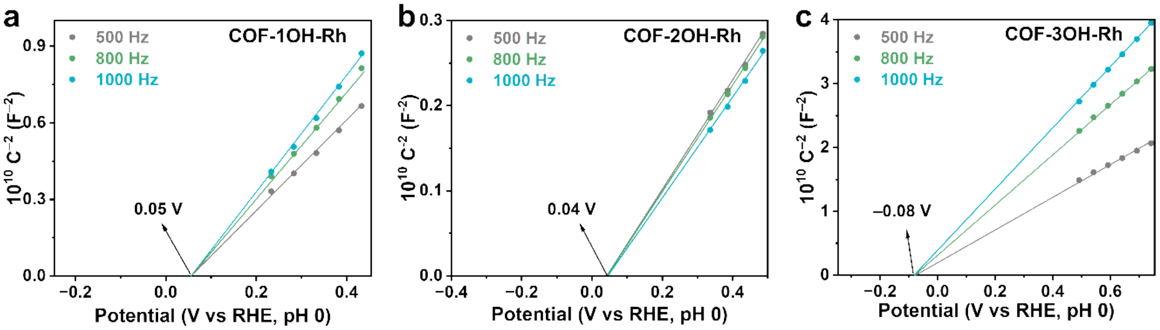

Fig. S16. Mott–Schottky diagrams of COF-1OH-Rh (a), COF-2OH-Rh (b) and COF-3OH-Rh (c).

Mott-Schottky measurements indicate n-type semiconductor characteristics for all three materials, evidenced by the positive slopes of the corresponding plots (Fig. S16).[13,14] Their conduction band (CB) potentials are estimated to be approximately 0.3 V below the flat-band potential, located at –0.25, –0.26 and –0.38 V, respectively.

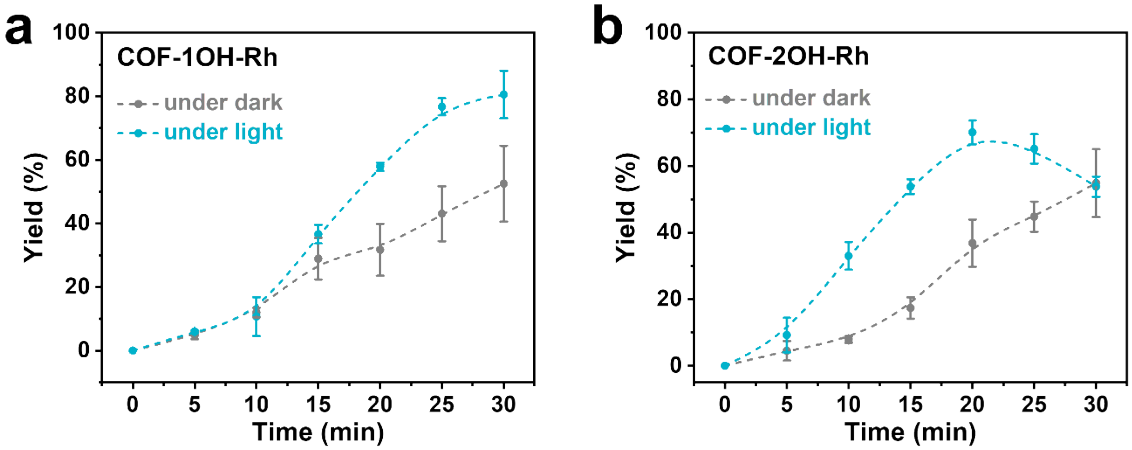

Fig. S17. NADH regeneration kinetics of COF-1OH-Rh (a) and COF-2OH-Rh (b) under dark and light conditions.

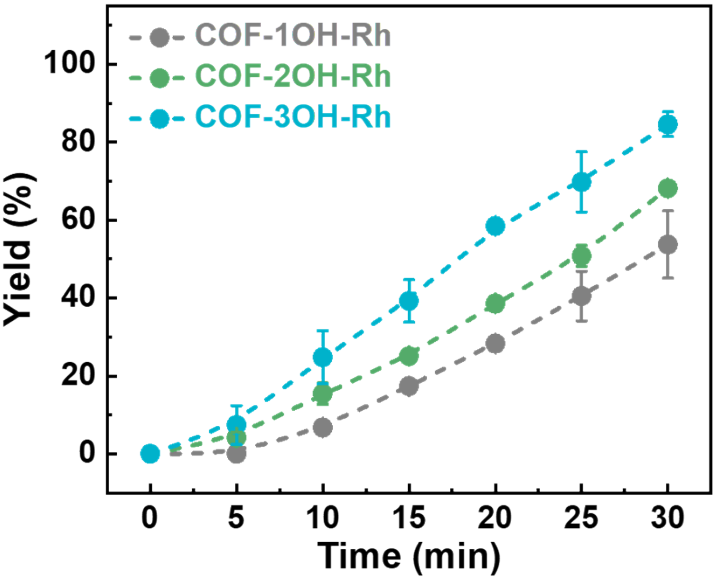

Fig. S18. Comparison of NADH regeneration kinetics under light conditions for COF-xOH-Rhs.

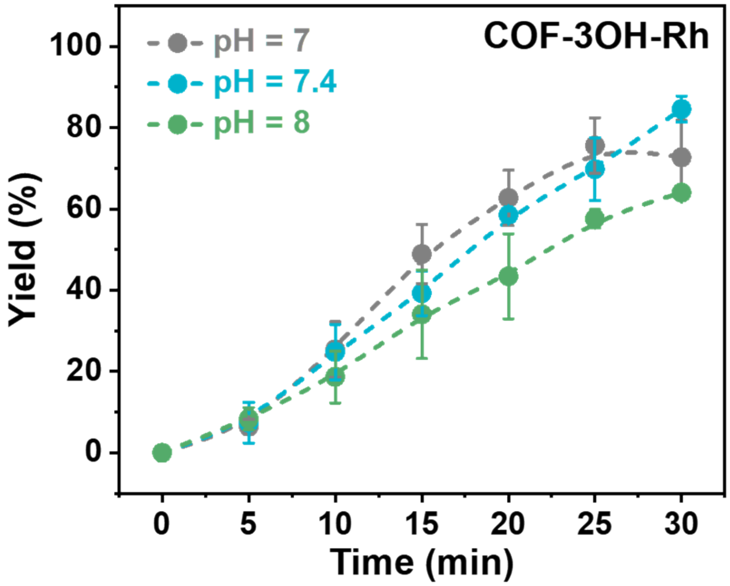

Fig. S19. Comparison of NADH regeneration kinetics over COF-3OH-Rh under illumination at pH 7.0, 7.4 and 8.0.

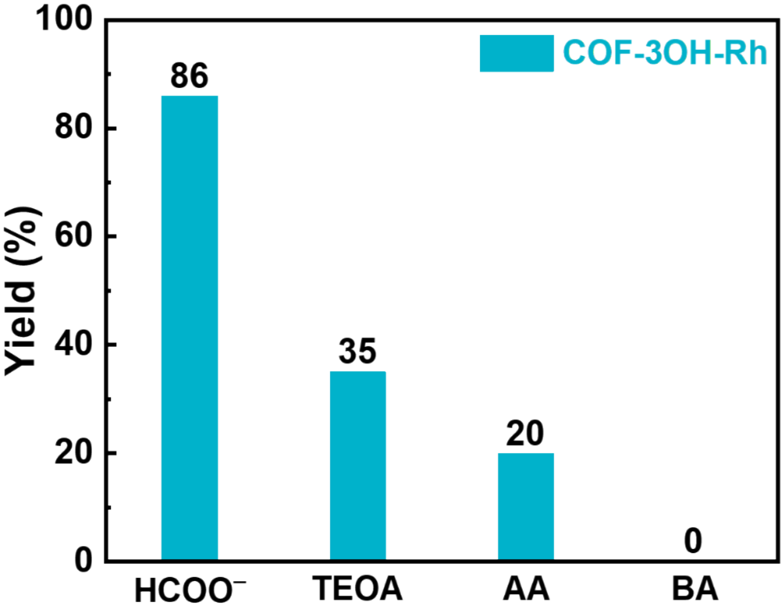

Fig. S20. NADH yields of COF-3OH-Rh under light with different sacrificial reagents after 30 min.

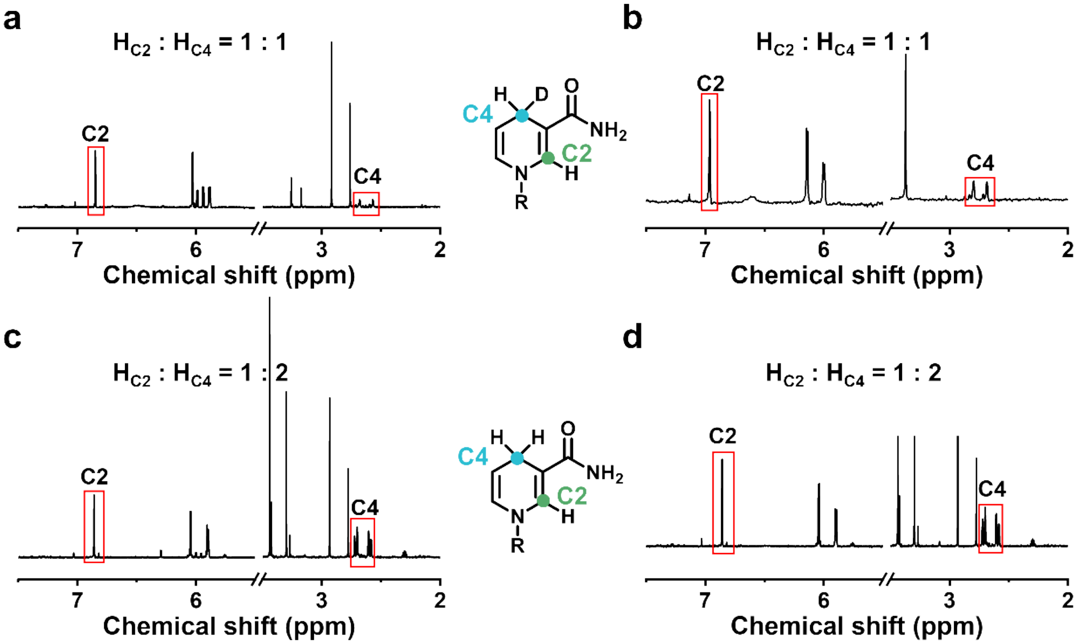

Fig. S21. Isotopic labeling experiments. (a, b) ^{1}H-NMR spectra of NADH obtained from COF-3OH-Rh after 30 min in DCOONa solution under dark (a) and light (b) conditions. (c, d) ^{1}H-NMR spectra obtained from COF-3OH-Rh after 30 min in D_2O with HCOONa under dark (c) and light (d) conditions.

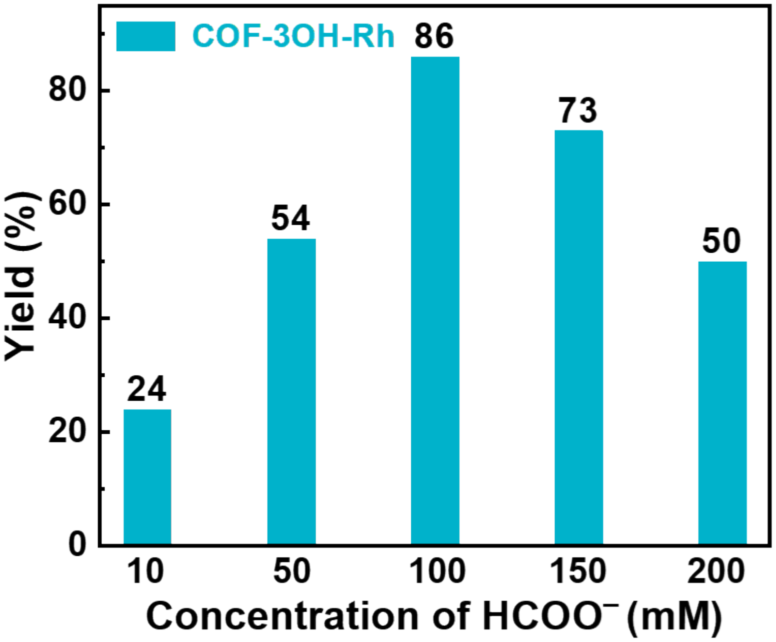

Fig. S22. NADH yields of COF-3OH-Rh under light at different formate concentrations after 30 min.

The NADH regeneration efficiency exhibited a clear dependence on HCOONa concentration, increasing with concentration up to 100 mM and then decreasing at higher concentrations.

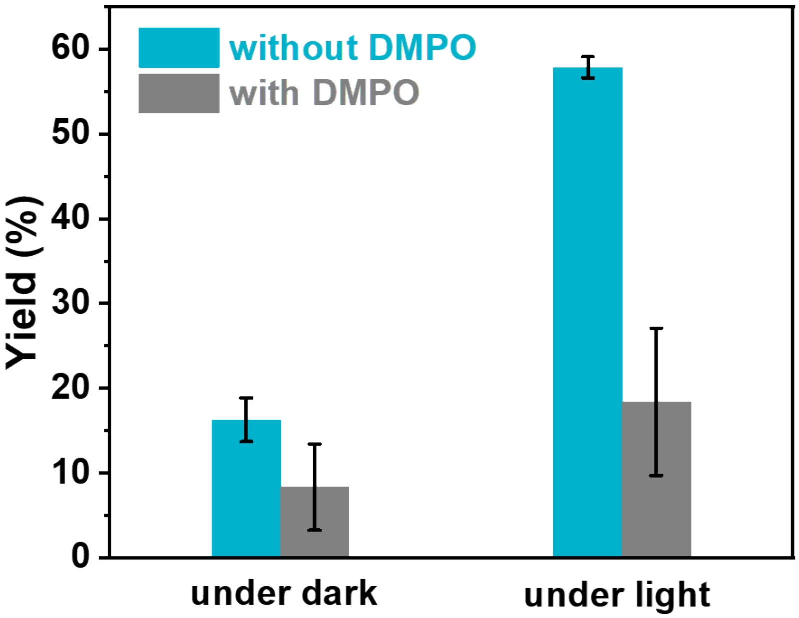

Fig. S23. Influence of DMPO as a radical-trapping agent on the NADH regeneration rate over COF-3OH-Rh after 20 min under dark and light conditions.

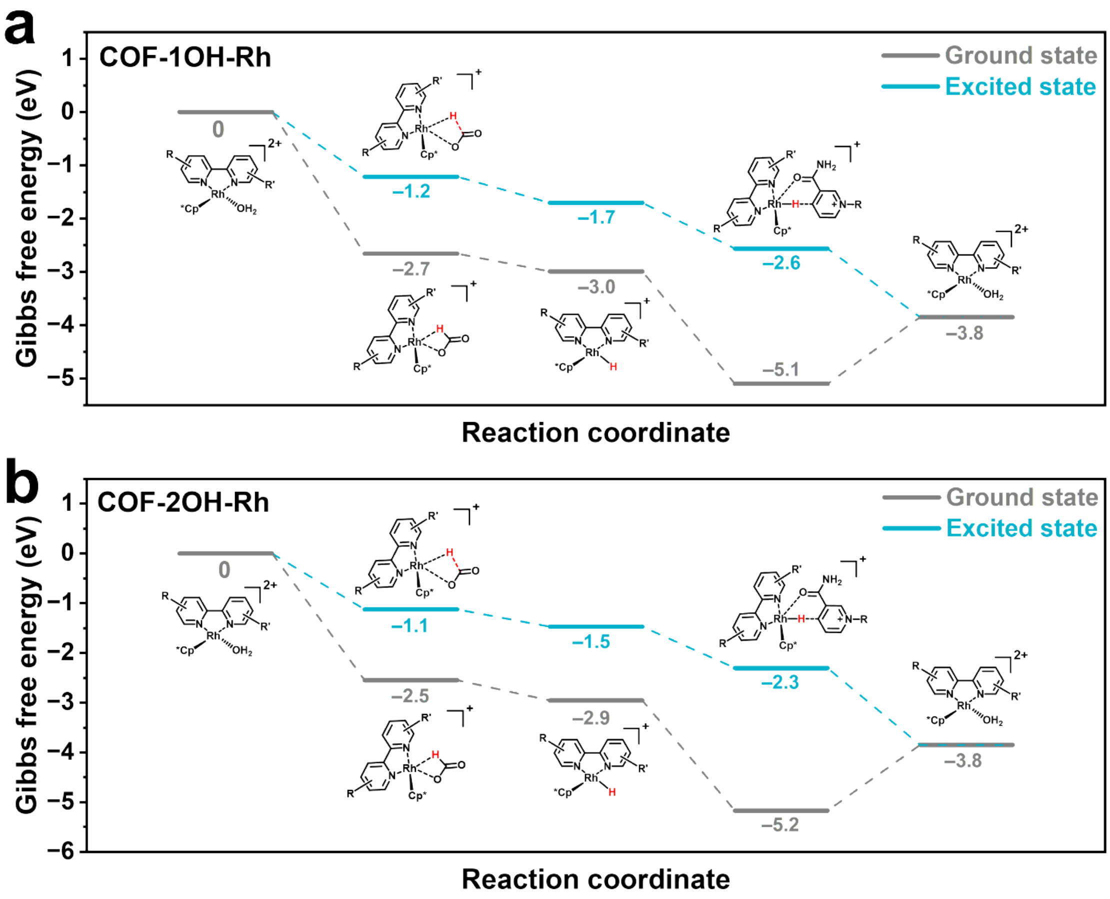

Fig. S24. Gibbs free energy of NADH regeneration at the Rh site of COF-1OH-Rh (a) and COF-2OH-Rh (b).

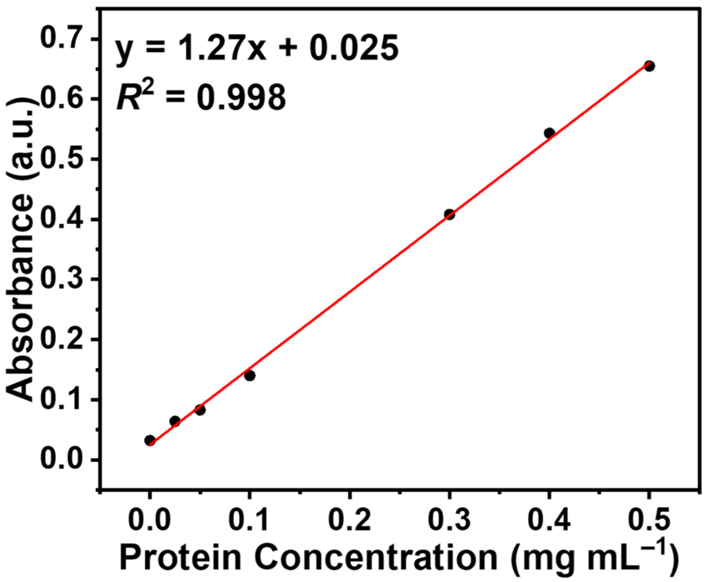

Fig. S25. Standard curve for protein concentration determination in supernatant using an Enhanced BCA Protein Assay Kit (Beyotime), measured with UV–Vis spectrophotometry.

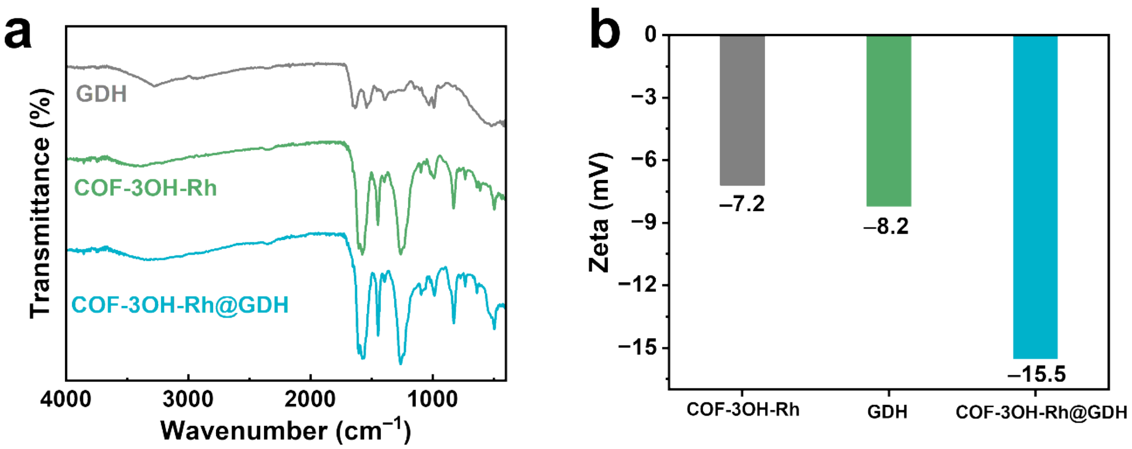

Fig. S26. FT-IR spectra (a) and Zeta potential plots (b) of free GDH, COF-3OH-Rh and COF-3OH-Rh@GDH.

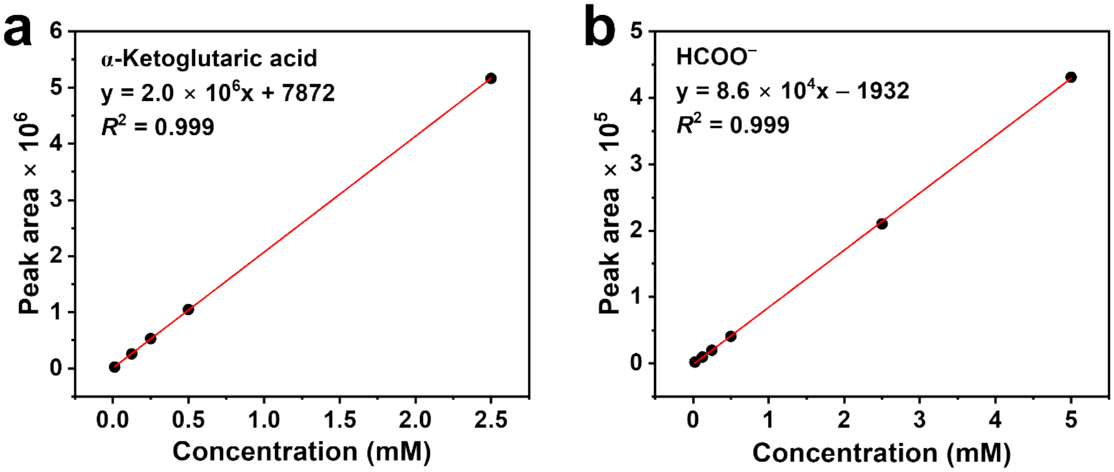

Fig. S27. Standard curve for α-ketoglutaric acid (a) and formate (b) concentrations determined by HPLC.

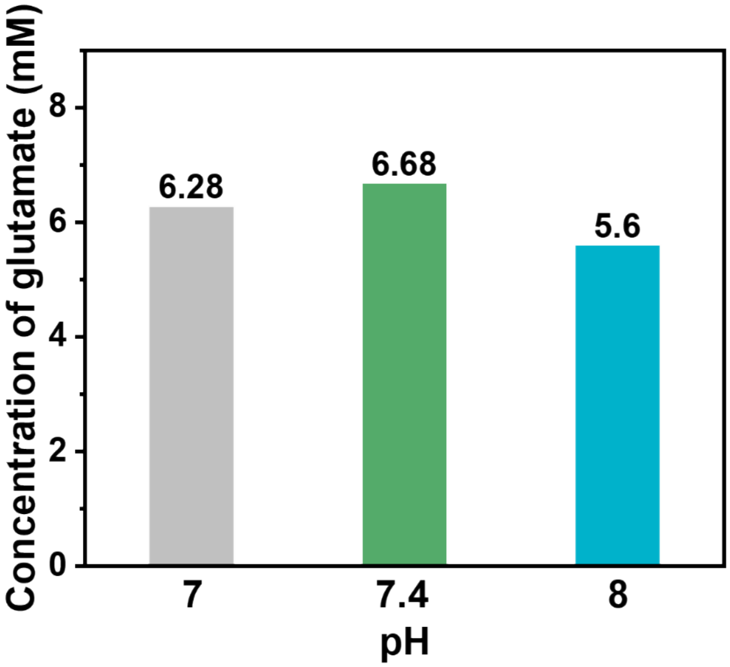

Fig. S28. Glutamate concentrations at 4 hours for COF-3OH-Rh@GDH under different pH conditions.

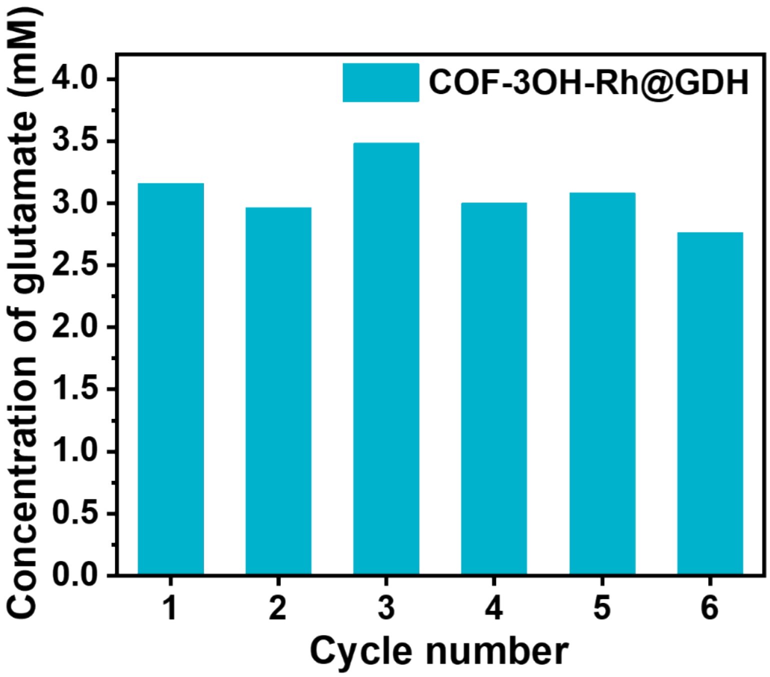

Fig. S29. Recycling stability of COF-3OH-Rh@GDH for glutamate synthesis after 2 hours under light over six consecutive runs.

Supplementary Table 1. Crystal cell parameter information for COF-xOH.

Parameters	COF-1OH	COF-2OH	COF-3OH
a	29.99	29.99	30.52
b	29.99	29.99	30.52
c	3.49	3.49	3.43
α	90	90	90
β	90	90	90
γ	120	120	120
R_p	0.56%	1.46%	0.79%
R_{wp}	0.77%	2.18%	1.26%

Supplementary Table 2. ICP-OES test results for catalysts with different Rh loading levels.

Catalyst Number	ICP Data (ppm)	Content (wt%)
1	0.39	1.95
2	1.31	6.50
3	0.68	3.40
4	0.73	3.65
5	0.88	4.40

Supplementary Table 3. Absorbance of proteins in the supernatant measured at 595 nm.

Number of washing cycles	Absorbance
1	0.051
2	0.010
3	0.007
4	0.008

Supplementary Table 4. Performance comparison of the COF-3OH-Rh@GDH system versus state-of-the-art chemo-enzymatic platforms for glutamate synthesis.

Catalyst	NADH regeneration								Chemo-enzymatic synthesis							
	Catalytic method	V (mL)	Catalyst dosage	$C_{0\ \mathrm{NAD}^+}$ (mM)	Compatibility	t_1 (min)	Y_{NADH} (%)	$S_{1,4\text{-}\mathrm{NADH}}$ (%)	Enzyme dosage (U)	$C_{1\ \mathrm{NAD}^+}$ (mM)	$C_{2\mathrm{k}}$ (mM)	t_2 (h)	C_g (mM)	$\mathrm{TON_g}$	$\mathrm{TOF_g}$ (h^{-1})	Ref.
Rh-PCN	Photocatalysis	2	2 mg	1	TEOA	6	75.0	100	/	1	/	0.67	2.2	2.20	3.33	15
COF-T3	Photocatalysis	/	3 mg/mL	1	TEOA	20	89.0	100	160	1	/	1.67	4.1	4.10	2.46	16
PCN@PDBTS-HN	Photocatalysis	/	1 mg/mL	0.67	TEOA	40	85.4	100	45	1.34	10	12	8.39	6.26	0.52	17
RH-vi^{2+}@PTTH	Photo-electrocatalysis	15	0.44 mg	0.5	H_2O	180	25.5	100	750	0.5	0.5	1	0.07	0.14	0.14	18
CFP	Photo-electrocatalysis	2	/	1	H_2O	30	60.0	100	/	1	80	56	72	72.00	1.29	19
Rh-bpy-MS@GDH	Electrocatalysis	80	40 mg	1	H_2O	60	81.0	100	625	12.5	375	4	32.6	2.61	0.65	20
COF-3OH-Rh	Light Promotion	2.5	3.5 mg	1	$HCOO^-$	30	87.0	100	155	1	20	8	14.18	14.18	1.77	This work

Note: V represents the total reaction volume; C_0 represents the initial NAD^+ concentration added in the NADH regeneration reaction; t_1 represents the time used for the NADH regeneration reaction; Y_{NADH} represents the NADH regeneration yield; $S_{\text{1,4-NADH}}$ represents the selectivity of 1,4-NADH; C_1 NAD^+ represents the initial NAD^+ concentration added in the chemoenzymatic synthesis reaction; C_{2k} represents the initial concentration of ketoglutarate added in the chemo-enzymatic synthesis reaction; t_2 represents the time used for the chemo-enzymatic synthesis reaction; C_{g} represents the final concentration of glutamate; TON_{g} and TOF_{g} represent the turnover number and turnover frequency of the glutamate synthesis reaction, calculated based on cofactor consumption.

References

1 J. Hutter, M. Iannuzzi, F. Schiffmann, and J. VandeVondele, *WIREs Comput. Mol. Sci.*, 2014, **4**, 15–25.

2 J. P. Perdew, K. Burke, and M. Ernzerhof, *Phys. Rev. Lett.*, 1996, **77**, 3865–3868.

3 S. Grimme, *J. Comput. Chem.*, 2006, **27**, 1787–1799.

4 S. Goedecker, M. Teter, and J. Hutter, *Phys. Rev. B*, 1996, **54**, 1703–1710.

5 C. Hartwigsen, S. Goedecker, and J. Hutter, *Phys. Rev. B*, 1998, **58**, 3641–3662.

6 J. VandeVondele, and J. Hutter, *J. Chem. Phys.*, 2007, **127**, 114105.

7 T. Lu, and F. Chen, *J. Comput. Chem.*, 2012, **33**, 580–592.

8 T. Lu, *J. Chem. Phys.*, 2024, **161**, 082503.

9 Y. Chen, X. Luo, J. Zhang, L. Hu, T. Xu, W. Li, L. Chen, M. Shen, S.-B. Ren, D.-M. Han, G.-H. Ning, and D. Li, *J. Mater. Chem. A*, 2022, **10**, 24620–24627.

10 J. Wang, W. Zhu, F. Meng, G. Bai, Q. Zhang, and X. Lan, *ACS Catal.*, 2023, **13**, 4316–4329.

11 Z. Cheng, P. Zhang, Z. Wang, H. Jiang, W. Wang, D. Liu, L. Wang, G. Zhu, and X. Zou, *Small*, 2023, **19**, 2300438.

12 Z. Chen, J. Wang, M. Hao, Y. Xie, X. Liu, H. Yang, G. I. N. Waterhouse, X. Wang, and S. Ma, *Nat. Commun.*, 2023, **14**, 1106.

13 D. Jiang, Z.-L. Wang, Y.-Z. Cheng, Y.-X. Yu, H.-Y. Kong, X.-Y. Bian, X.-M. Dou, S.-L. Li, D.-H. Yang, X. Ding, and B.-H. Han, *Chem. Eng. J.*, 2024, **497**, 154212.

14 Y. Cheng, X. Bao, D. Jiang, W. Ji, D. Yang, X. Ding, X. Liu, Y. He, and B. Han, *Angew. Chem. Int. Ed.*, 2025, **64**, e202414943.

15 C. Tao, Z. Wang, Y. Dai, S. Zhang, J. Li, Y. Chen, X. Mao, J. Shi, and Z. Jiang, *Angew. Chem. Int. Ed.*, 2025, **64**, e202424995.

16 L. Tong, Z. Gong, Y. Wang, J. Luo, S. Huang, R. Gao, G. Chen, and G. Ouyang, *J. Am. Chem. Soc.*, 2024, **146**, 21025–21033.

17 S. Wang, X. Wu, J. Fang, F. Zhang, Y. Liu, H. Liu, Y. He, M. Luo, and R. Li, *ACS Catal.*, 2023, **13**, 4433–4443.

18 Z. Zhao, Y. Wu, C. Liu, Y. Li, C. Gong, H. Ning, P. Zhang, F. Li, L. Sun, and F. Li, *Adv. Sci.*, 2025, **12**, 2413668.

19 J. Kim, J. Jang, T. Hilberath, F. Hollmann, and C. B. Park, *Nat. Synth.*, 2022, **1**, 776–786.

20 C. Wang, W. Dong, P. Zhang, Y. Ma, Z. Han, Y. Zou, W. Wang, H. Li, F. Hollmann, and J. Liu, *Angew. Chem. Int. Ed.*, 2024, e202408756.